AEgIS experiment at CERN: design and commissioning of SARA (Scintillator Assemblies to Reveal Annihilations)

Published by IOP Publishing for Sissa Medialab

Received: *June 11, 2025*
Revised: *September 1, 2025*
Accepted: *October 7, 2025*
Published: *January 21, 2026*

AEgIS experiment at CERN: design and commissioning of SARA (Scintillator Assemblies to Reveal Annihilations)

P. Conte[a,b,*] **G. Consolati**[a,b] **M. Prata**[c] **M. Berghold**[d] **R. Caravita**[e] **R. Ferguson**[e,f] **M. Grosbart**[g] **F. Guatieri**[d,e,f] **S. Haider**[g] **G. Khatri**[g] **L. Lappo**[h] **P. Moskal**[i,j] **M. Münster**[d] **L. Penasa**[e,f] **and S. Sharma**[i,j]

[a] *INFN Milano, via Celoria 16, 20133 Milano, Italy*
[b] *Department of Aerospace Science and Technology, Politecnico di Milano, via La Masa 34, 20156 Milano, Italy*
[c] *INFN Pavia, via Bassi 6, 27100 Pavia, Italy*
[d] *Heinz Maier Leibnitz Zentrum (MLZ), Technical University of Munich, Lichtenbergstraße 1, 85748, Garching, Germany*
[e] *TIFPA/INFN Trento, via Sommarive 14, 38123 Povo, Trento, Italy*
[f] *Department of Physics, University of Trento, via Sommarive 14, 38123 Povo, Trento, Italy*
[g] *Physics Department, CERN, 1211 Geneva 23, Switzerland*
[h] *Faculty of Physics, Warsaw University of Technology, ul. Koszykowa 75, 00-662, Warsaw, Poland*
[i] *Marian Smoluchowski Institute of Physics, Jagiellonian University, ul. Łojasiewicza 11, 30-348 Kraków, Poland*
[j] *Centre for Theranostics, Jagiellonian University, ul. Kopernika 40, 31-501 Kraków, Poland*

E-mail: pietro.conte@mi.infn.it

Abstract: SARA is the system of plastic scintillators coupled with silicon photomultipliers that will take part in the AEgIS experiment at CERN, measuring the time-of-flight of antihydrogen as it falls through a moiré deflectometer. Its development focused on simplicity, versatility and economy of the design and was supported by both physical tests and numerical simulations. The instrument structure pairs the utilization of the scintillators as structural components with custom made 3D printed corner elements and the electronics allows selection between coincidence discrimination made on each scintillator and made between different scintillators.

Keywords: Beam-line instrumentation (beam position and profile monitors, beam-intensity monitors, bunch length monitors); Detector design and construction technologies and materials; Photon detectors for UV, visible and IR photons (solid-state) (PIN diodes, APDs, Si-PMTs, G-APDs, CCDs, EBCCDs, EMCCDs, CMOS imagers, etc); Scintillators and scintillating fibres and light guides

In memory of Sara Conte

*Corresponding author.

https://doi.org/10.1088/1748-0221/21/01/P01022

Contents

1 Introduction

The AEgIS experiment (Antihydrogen Experiment: gravity, Interferometry, Spectroscopy) at CERN aims to measure the effects of Earth's gravity on antimatter in the absence of magnetic field influences, with an accuracy of 1% [1]. The results will pave the way for testing the Weak Equivalence Principle of General Relativity and the Charge, Parity and Time Reversal Symmetry embedded in Quantum Field Theory [2].

The experiment will use a horizontally-boosted, free-falling pulsed beam of antihydrogen ($\bar{H}$), which will be sent through a moiré deflectometer contained within a horizontal tube maintained under ultra-high-vacuum conditions. Two horizontal gratings, whose relative positions can be tuned, are placed at the entrance and at the midpoint of the tube, perpendicular to its axis. They generate a periodic spatial distribution of antihydrogen at a fixed distance downstream of the second grid, since only antiparticles following nearly horizontal trajectories avoid colliding and annihilating with the gratings (figures 1(a) and (b)).

This apparatus differs from a Mach-Zehnder atom interferometer, that operates in a regime where the de Broglie wavelength λ is much larger than the grating period d, and where three identical gratings are placed at an equal distance L from each other. On the third one, an interference pattern is produced, showing the same period as the gratings [3, 4]. In the presence of gravity, this pattern is shifted vertically by a distance equal to:

$$\Delta y = -g\Delta t^2 \tag{1.1}$$

where g is the local gravitational acceleration and $\Delta t = v/L$ is the time-of-flight of a particle beam moving at velocity v between two gratings. The use of a Mach-Zehnder interferometer is problematic in the presence of antimatter due to various decoherence effects. More important, the divergence of the

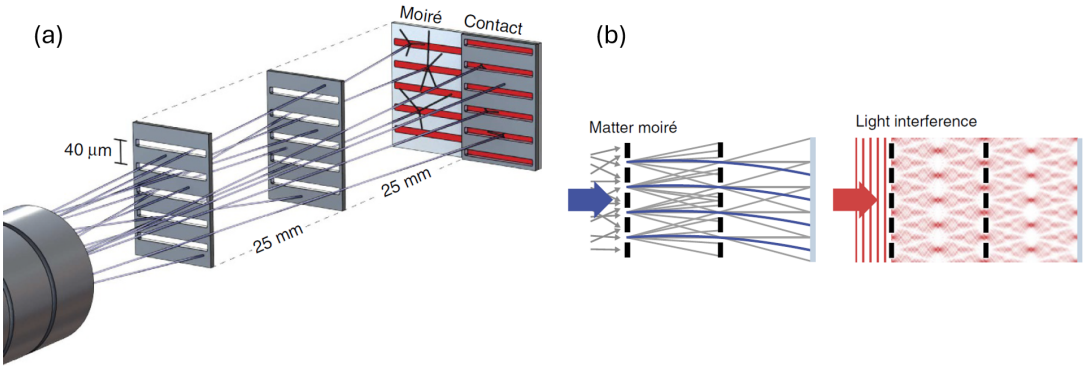

Figure 1. (a,b) Deflectometer functioning principle, where antihydrogen atoms pass through two gratings and form a fringe pattern. Reproduced from [5]. CC BY 4.0.

antiatom beam must be less than the diffraction angle $\alpha = \lambda/d$. A way to circumvent this limitation is indeed to operate the device in the moiré regime, where $\alpha \ll d/L$, and consequently the diffractive effects are replaced by a classical shadow pattern of the antiatoms. Once past the two gratings, the latter converges on a final detector (either a third grating and a counter, as for the Oberthaler original configuration [6], or a position-sensitive detector, as for the AEgIS experiment). Nevertheless, the law of motion of the free-falling atoms (eq. (1.1)) is valid in both regimes.

In the present setup, the fringe pattern — a fringe-like distribution of annihilation points — obtained after the second grating will be collected by OPHANIM, a high-resolution, position-sensitive, 3840-Megapixel CMOS detector [7] capable of comparing the antihydrogen fringe pattern with the one of a reference light source, which has traveled the same path and has been negligibly affected by gravity.

The vertical position difference measured by the detector will be used in the equation $\Delta y = -\bar{g}\Delta t^2$ (derived from eq. (1.1)), yielding the intensity of the gravitational acceleration acting on antimatter $\bar{g}$. The antihydrogen transit time will be measured as the difference between the time instant of its arrival at OPHANIM and the one of its formation, known with an uncertainty of 250 ns [8]. Antihydrogen will be obtained by exploiting the interaction between antiprotons, coming from the Antimatter Decelerator (AD), and excited positronium in Rydberg states (Ps^*), generated by shooting two laser beams (205.045 nm and 1693 nm) toward a cloud of ortho-positronium. The latter will be formed through the interaction between a positron beam, coming from a ^{22}Na source, and a nanochanneled silicon target [9]. This antihydrogen production is called charge-exchange process and can be summarized by the equation [10]:

$$Ps^* + \bar{p} \rightarrow \bar{H}^* + e^- \tag{1.2}$$

This paper presents and discusses SARA (Scintillator Assemblies to Reveal Annihilations), the system of scintillators that aims to measure the time-of-flight distribution of antihydrogen atoms as they move through the moiré deflectometer of the AEgIS apparatus (figure 2(a) and (b)). Timing measurements are essential for determining the gravitational acceleration of antimatter and will be performed by detecting the annihilation products generated by the interaction between a fraction of the antiatoms with the two gratings and with OPHANIM.

2026 JINST 21 P01022

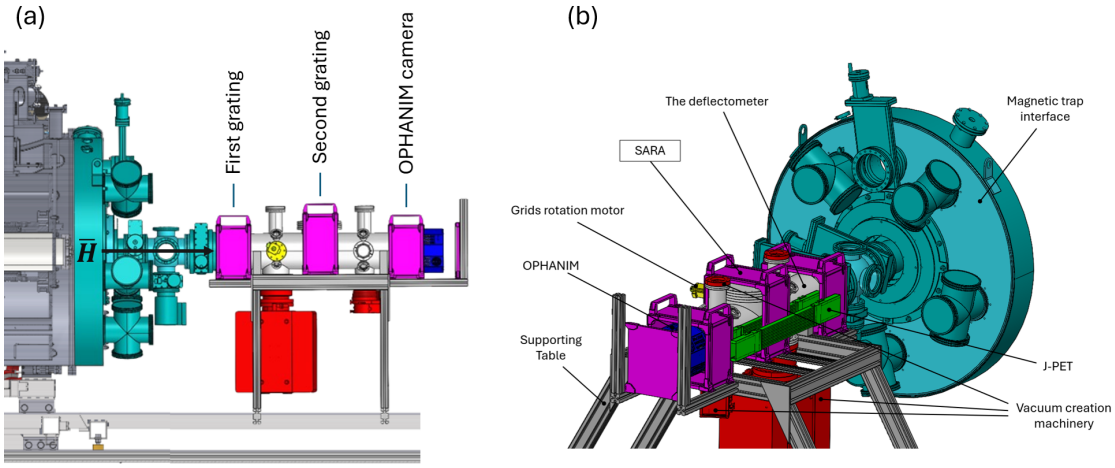

Figure 2. (a) Gravity Module of the AEgIS apparatus, where the pink boxes indicate the scintillator assemblies (SARA modules) positioned around the gratings and OPHANIM. (b) The complete Gravity Module layout, in which the pink boxes represent scintillator assemblies and the green slabs correspond to the planned J-PET modules [11].

2 Objective and requirements

As anticipated, the main goal of the SARA detector is to measure the time-of-flight Δt distribution of antihydrogen atoms by detecting their annihilation products (in particular pions) generated when they collide with either one of the two moiré gratings or the OPHANIM detector surface. This data will allow working out g from eq. (1.1) in combination with the vertical deflection Δy measurement by the OPHANIM detector. In addition, the number of annihilations produced on the two grids and recorded by SARA will enable estimation of the fraction of $\bar{H}$ produced that do not reach the final CMOS detector, providing information on the temporal spread of the antihydrogen beam and the transmittivity of the individual gratings. The 1% accuracy goal depends on both the minimal velocity of the antihydrogen beam and the accumulated statistics (i.e., the total number of antiatoms reaching the final detector, and therefore on the production efficiency), making it crucial for the SARA detector to detect antihydrogen annihilations with high efficiency.

The SARA detector was henceforth designed following four paradigms:

1. The detector shall clearly distinguish the annihilations occurring at the two gratings and at OPHANIM separately, so it must be composed of at least three independent modules.

2. Each module must be able to detect the majority of annihilation events happening at the assigned annihilation site. Therefore, each module shall detect the majority of the pions produced during the nucleon-antinucleon annihilation, so their efficiencies have to be higher than 50%, to be in line with the 58% efficiency of the OPHANIM detector and not impose more stringent requirements on the antihydrogen source flux.

3. The time resolution of each detecting element of the modules should be on the order of 10 ns, to allow a measurement of the $\bar{H}$ time-of-flight at the same order-of-magnitude accuracy as their formation instant, defined by laser pulse duration (4–5 ns), and the spread in time-of-flight of the Ps^* atoms in the antiproton cloud (10–50 ns).

2026 JINST 21 P01022

4. The SARA detector should allow rejecting dark counts, cosmic-ray muons and natural radioactivity of the laboratory by enabling formation of coincidences, ensuring that the events originating in its encompassed volume are easily distinguishable.

3 Detector design

3.1 Initial design assumptions

Starting from the requirements outlined above, a combination of plastic scintillators and Silicon Photomultipliers (SiPMs) was adopted, since it is an effective technological choice to reveal annihilations. The former were chosen both for their fast rise time (often below 1 ns), their high detection efficiency and their reduced costs in encompassing large volumes. According to the results of the ATRAP Experiment [12], a thickness of around 1 cm generates a sufficient amount of photons during the transit of pions produced by annihilation. On the other hand, the SiPMs were selected after a trade off against photomultiplier tubes (PMTs) as alternative. Even though PMTs offer superior performance in terms of dark count rates at room temperature, SiPMs are notoriously insensitive to magnetic fields [13], observable in the surrounding of SARA due to the nearby presence of the 1 T and 5 T magnets in the main AEgIS cryostat. Indeed, in the nearby region magnetic fields of around 1 mT were measured, which can therefore influence the gain of a PMT while having no effect on SiPMs. The deflectometer will, however, be protected by suitable mumetal shields to avoid affecting the trajectories of the antihydrogen atoms. This means that, unlike PMTs, SiPMs do not require complex shielding, keeping the detector footprint compact. In addition, PMTs usually require cumbersome light guides, which would need more space than that actually available between adiacent scintillators (around 25 cm), unless one resorts to rather complex geometries.

In order to maximize the detection efficiency and effectively minimize the atmospheric muon background noise, while keeping the design as simple as possible, twelve rectangular plastic scintillators were assembled in three boxes to be placed around the gratings and the OPHANIM detection surface, partially covering the solid angle around them. An additional rectangular scintillator panel was placed behind the final detector to enhance its solid angle coverage; the final assembly and placement are shown in figure 3(b). The need of performing baking procedure in order to obtain ultra-high vacuum inside the tube, coupled with the high sensitivity of the selected scintillator material to high temperatures (see subsection 3.2), imposed the definition of a box architecture that allows fast integration and removal procedures. A test was performed to determine whether the application of mica insulation layers between the deflectometer and the scintillators could prevent material damages. However, it was found that it is impossible to leave SARA intact during the baking. Consequently, the chosen boxes architecture consists of two parts: an upper section, containing the two vertical and the upper horizontal scintillators, and a lower section, containing the remaining panel (figure 3(a)). The choice to divide each box in two sections allows a fast removal (and subsequent mounting) when a baking process for the whole deflectometer is needed. This ensure that the two procedures will not be a bottleneck of the experiment execution. To integrate the boxes on the instrument, first the lower part is placed in its correct position and then the upper part is lowered from above. Finally, the two parts are fastened both together and to the instrument supporting structure by applying four screws at the four bottom corners of the created box.

2026 JINST 21 P01022

The whole deflectometer apparatus, including SARA, will lay on a single supporting table made of Bosch profiles with various section dimensions. In particular, each box of scintillators, after the integration in the moiré deflectometer, will be supported by two horizontal and parallel beams with section variable between $20 \times 20\,\mathrm{mm}^2$, $30 \times 30\,\mathrm{mm}^2$ and $45 \times 45\,\mathrm{mm}^2$ sizes. In addition, the final panel will be supported by one or two horizontal beams plus two vertical beams for stability, therefore SARA has been designed to guarantee adaptability to various Bosch profiles section dimensions and to horizontal supporting beams orientation parallel or orthogonal to the deflectometer axis.

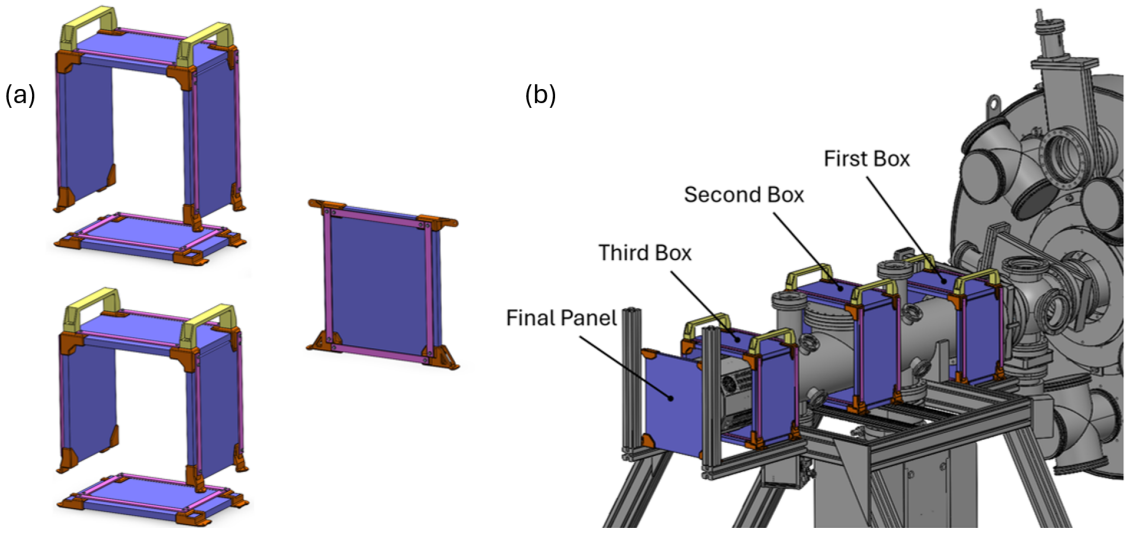

Figure 3. (a) Big box and one small box showing the two parts architecture; on the right the final panel, (b) SARA integrated in the AEgIS apparatus.

3.2 Scintillator properties

The material selected to create the scintillators is the general purpose BC-404 from Luxium Solutions, of which some 1 m long, 277 mm wide, 13 mm thick panels were already available and whose properties are collected in table 1.

Table 1. Properties of BC-404 scintillator [14, 15]. Reproduced with permission from [14].

Property	Value
Name:	Luxium Solutions BC-404
Base:	Polyvinyl-toluene
Panels dimensions (mm):	$1000 \times 277 \times 13.3$
Refractive index:	1.58
Softening point (°C):	70
Rise time (ns):	0.7
Decay time (ns):	1.8
Wavelength of max. emission (nm):	408
Light attenuation length (cm):	140
Light output (n. photons/MeV):	10800

2026 JINST 21 P01022

Given the limited space around the deflectometer, the on-axis dimension of the boxes scintillator panels was fixed to 200 mm and their last dimension was determined according to the detector system surrounding. Moving to the thirteenth panel (placed behind OPHANIM), its dimensions were derived from the starting BC-404 material panels plus the decision of having this scintillator centered on the deflectometer axis. Concerning the sizes, all the horizontal scintillators of the boxes are 316 mm long, the second box has vertical scintillators 316 mm high and the first and third boxes have vertical scintillator panels 270 mm high. On the other hand, the final scintillator is 275 mm wide and 318 mm high. A simple Monte Carlo simulation was exploited to estimate the fraction of the solid angles around each annihilation region that SARA is able to cover. In particular, it considered 10^6 randomly generated directions per annihilation site and approximated the latter as the points of intersection between the gratings or OPHANIM and the deflectometer axis. In addition, the analysis computed the cross detection (e.g., annihilation products generated at the first grating and detected by the second box), finding it is negligible. The results are reported in table 2 and figure 4.

The solid angles coverage computed, coupled with the second requirement presented in section 2, led to the finding of a minimum acceptable value for the scintillator panel efficiencies. In particular, for the first box a minimum averaged efficiency of 0.755 was found, for the second a minimum averaged value of 0.780 was calculated and for the third box plus final panel assembly a minimum averaged efficiency of 0.703 was computed.

Table 2. Solid angle fractions around the three annihilation sites that are covered by the three modules.

Annihilation site	Module considered	Solid angle fraction (%)
First grating	First box	66.2
Second grating	Second box	64.1
OPHANIM	Third box and final panel	71.1
First grating	Second Box	1.41
First grating	Third box and final panel	0.96
Second grating	First box	1.21
Second grating	Third box and final panel	1.97
OPHANIM	First box	0.16
OPHANIM	Second box	1.37

3.3 Detector mechanical design

Given the thickness of the scintillator panels, they have been exploited as structural elements for the boxes, obtained by connecting the panels by means of custom 3D printed corner elements, by some aluminum bars and two handles. The material selected to 3D print the corner elements is Nylon PA12 [16], chosen for its good mechanical properties over economic cost ratio, and the printing technology selected was the Multi Jet Fusion, that guarantees good isotropy of the final products. A trade-off analysis was conducted to compare a plastic 3D printed corner elements solution with a design obtained by welding metal plates. Although it would have been more economical, the latter solution was discarded because of the long-term damage at the points of contact between the scintillators and the metal plates edges. In addition, the first alternative had also the advantage of minimizing the overall detector weight, important for its supporting structure architecture.

2026 JINST 21 P01022

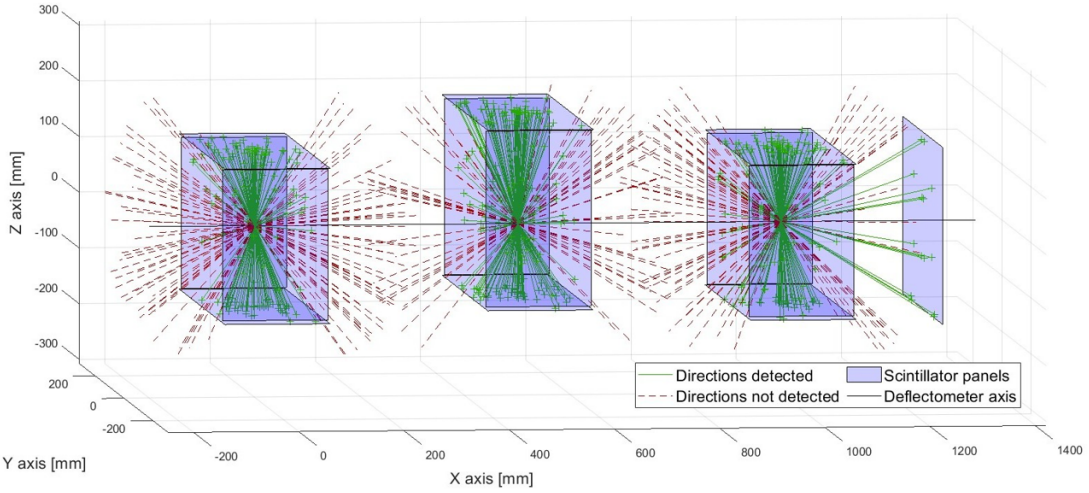

Figure 4. Monte Carlo simulation used to determine the solid angle fraction of each SARA module. The green lines are the directions revealable by the detector modules while the red dotted lines are directions not revealed by the module placed around their generation point.

The shape of the corner elements was determined according to their structural function, their role in protecting the scintillators corners from accidental impacts, the minimization of their mass and the simplicity of the 3D printing process. Furthermore, the design process focused on the realization of as many identical components as possible, feature that allowed to reduce their unit cost. The result is shown in figure 5(a).

Moving to the aluminum bars and handles, which hold the corner elements in place and facilitate handling, they have both been selected among COTS (Commercial-Off-The-Shelf) products. Aluminum 6060 T5, 15×3 mm section, 2 m long bars have been considered; for the latter, the Elesa M.443/200-CH-C9 handles were chosen. To connect corner elements, aluminum bars and handles, the former have been equipped with ensats, brass cylindrical inserts with a thread on the inside and designed to be hot-inserted in dedicated holes inside plastic components. The only disadvantage of this solution is to impose a minimum depth and walls thickness for the insertion holes, which slightly conflicts with the minimization of the printed material.

3.4 Finite elements mechanical simulations

In order to test the structural components before their physical realization, the whole design process was supported with mechanical finite elements analysis, using Autodesk Fusion as simulation software. In particular, the focus was directed to the central box, which is the bulkiest and so the one representing the critical case for the mechanical stresses. The analysis investigated four loading conditions characterized by the combination of weight (acting on every point of the structure) and a horizontal force (applied in a certain point of the structure), simulating both the nominal and the overloaded scenarios described in table 3.

In the first loading condition, the box, already fastened to the instrument supporting structure, is loaded with a horizontal force applied on one of its upper shorter horizontal edges. This load condition can also occur when only the upper part is fastened to the box supports and it simulates an accidental impact with the box after it has been integrated into the instrument. In the second and third cases, a hori-

2026 JINST 21 P01022

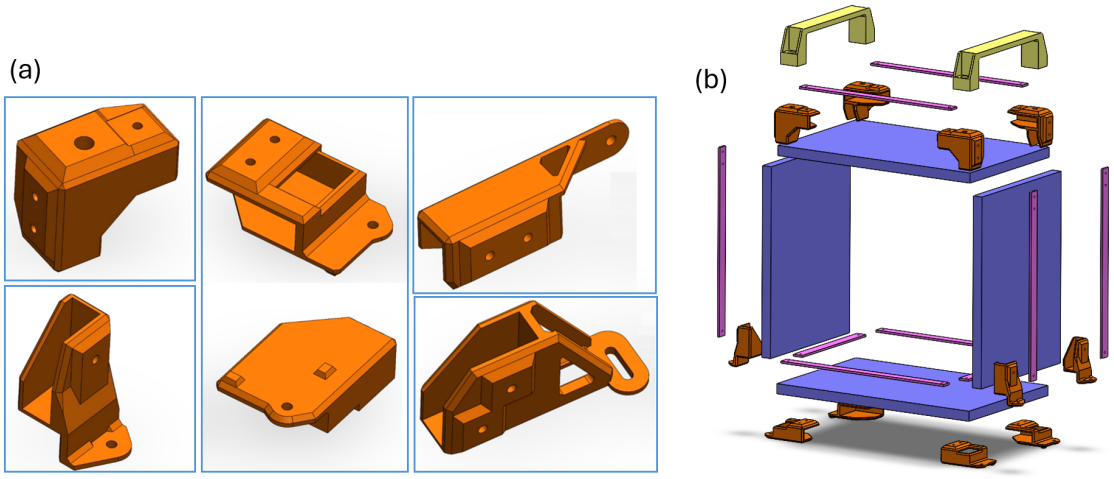

Figure 5. (a) The variants of corner elements, coming in two mirrored versions, as can be seen in the central image. (b) Exploded view of the first box.

Table 3. The two scenarios considered in the FEM analysis.

Quantity	Nominal scenario	Overloaded scenario
Weight W (N kg^{-1})	9.81	13.24
Horizontal force F (N)	10.0	15.0

zontal load is applied respectively inward and outward at a lower edge of the upper part. These two load combinations simulate an accidental impact that can happen during the upper part integration or removal. Finally, in the fourth load condition the central box is supported by two 20×20 mm^2 section Bosch profiles that run parallel to the deflectometer axis. In this case the gap between the two supporting beams is larger than the length of the lower horizontal scintillator, meaning that the whole box is sustained by the four horizontal flanges of the lower part corner elements only (the single holed flange appreciable in the central image of figure 5(a)). This last load combination does not take any horizontal force into account. Given the high elongation at break of Nylon PA12 (20%), maximum displacement was used as an indicator of stiffness. Indeed, the safety factor computed, evaluated as $SF = \sigma_Y / \sigma_W$, where σ indicates stresses, Y means Yield and W stands for Work, was always above 6. The results of the analysis, reported in figure 6 and table 4, show that the deformations can be considered reasonably acceptable.

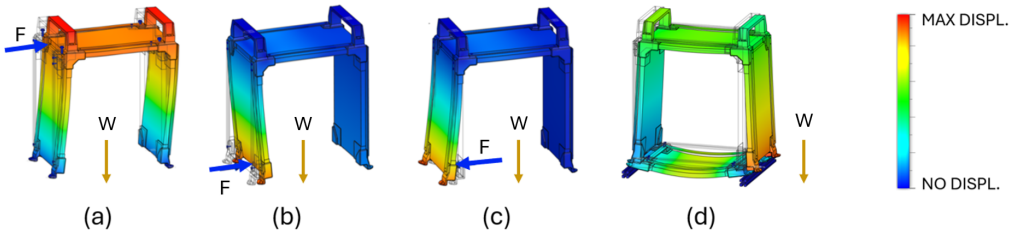

Figure 6. FEM analysis computed deformations. The blue arrows represent the applied force and gravity is always directed downward (the displacement is exaggerated for illustration purposes).

2026 JINST 21 P01022

Table 4. Maximum displacements computed with the FEM analysis.

Case	Nominal Scenario (mm)	Overloaded Scenario (mm)
(a)	0.443	0.670
(b)	0.997	1.497
(c)	1.659	2.497
(d)	0.122	0.133

3.5 Readout electronics

Concerning the electronics design, on every scintillator panel one PCB hosting twelve SiPMs was applied. The SiPMs were divided into two groups of six, each one equipped with a dedicated signal output port, with the possibility to read them either in coincidence or in parallel. It was initially decided to mount each PCB on one lateral side of the rectangular scintillators, using nylon screws as fastening strategy due to its reversibility, effectiveness and low cost. For this reason, the PCBs have been designed to be elongated, as wide as the thickness of the scintillators and equipped with four screw holes. A preliminary test was performed to compare the average output amplitude of a PCB hosting 3 SiPMs first mounted on a lateral side of a SARA scintillator and then on one of its two main surfaces, as represented in figure 7(a). The high-energy particles source used was atmospheric muons and the result of the two acquisitions was practically identical. Consequently, the lateral mounting position was selected for the better cable management granted and based on the reasonable assumption that a SiPM applied on a lateral surface has a direct view on a wider volume of the scintillator with respect to one applied to a main surface. Afterwards, a test was carried out to determine how to create threaded holes in the scintillator panels; the result is shown in figure 7(b). It is possible to generate the holes, but the procedure developed is time-consuming and quite complex; moreover, any error could damage the entire scintillator panel due to its extreme sensitivity to heat. For this reason, it was concluded to use black adhesive tape as a still reversible and straightforward solution to secure the PCBs and to add an additional layer of stray light protection to the SiPMs. In particular, compressing tape pieces were applied to press the two SiPMs regions of the PCB onto the scintillator, and covering pieces closed the gap between the circuit board and the scintillator thus preventing light infiltrations; also the PCB screw holes were taped as well.

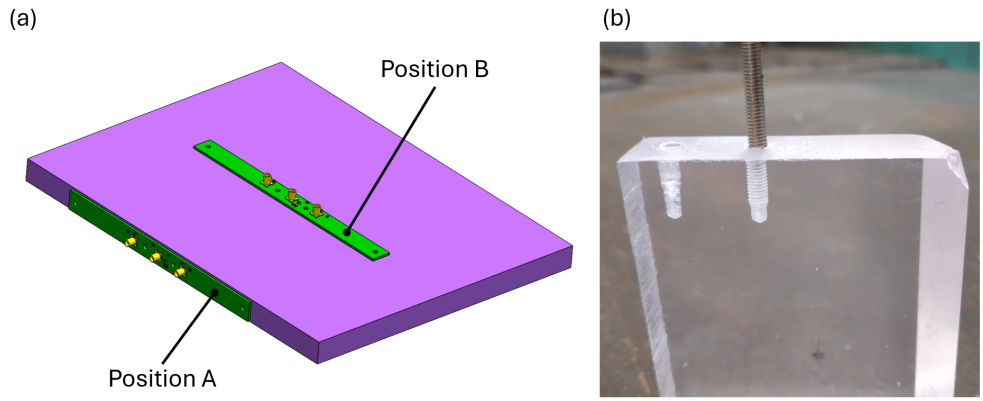

Figure 7. (a) The two PCB positions tested. (b) The result of the threaded hole creation test.

2026 JINST 21 P01022

The selected SiPM is the Hamamatsu S14160-3050HS. The choice was mainly driven by its peak sensitive wavelength, which closely matches the maximum emission wavelength of BC-404, and its compact dimensions ($3.4 \times 3.4 \times 1.35\,\mathrm{mm}^3$), tailored for the lateral side application.

The PCB architecture, shown in figure 8(a), is based on two channels, each consisting of six parallel SiPMs powered by a single supply line (J1 in the schematic shown in figure 8(a)) operating at 4 V above the breakdown voltage. After the power-line filtering stage, each channel includes a branch with a 100 nF discharging capacitor (C11 and C21 in figure 8(a)), which enables measurements of a single output signal as the voltage variation across a 1 kΩ series resistor (R11 and R21 in figure 8(a)). The goal for the PCB architecture design was to obtain a straightforward solution. In order to enable the 12 SiPMs in-parallel reading strategy, a short-circuit bridge can be obtained by applying a jumper to a central 3 pins connector (J2 in the figure). Moreover, due to the particular shape selected for the PCBs, the SiPMs have been arranged to form a pair of six elements strips aligned with the PCB main dimension (figure 8(b)). To improve the interaction between the detectors and the plastic scintillators, an optical grease (EJ-550 from Eljen Technology) was applied at their contact surface. Indeed, a test confirmed that, in the presence of grease and during the same amount of time, an increase in the number of detected scintillations caused by muons is observed.

Concerning the overall electronics setup, all the PCBs are powered by a single SiPMs power supply, the CAEN DT5485PB [17], exploiting a single input-13 output custom-made switch. All the PCBs outputs are collected by fast amplifiers with gain equal to 10, the CAEN N979 [18], that subsequently send the amplified signals to two or four 14-bit, 250 MS/s digitizers, the CAEN 5725SB [19], for data acquisition. Both the power and data lines use coaxial cables (RG174) with LEMO connectors. A representation of the electronics architecture is reported in figure 9.

It should be noted that the current design does not fully utilize the fast response capabilities of the selected SiPMs. Additionally, due to the developed circuit architecture, in which all six SiPMs in a line are connected in parallel, their outputs do not sum as expected. There are two possible reasons for this limitation. The first is that the activation of a single SiPM during a scintillation event induces a small voltage variation across the shared 100 nF capacitor, leading to different gain responses among the SiPMs. The second is the fact that connecting multiple SiPMs in parallel results in a higher overall capacitance, which affects the system signal characteristics. Nevertheless, the high number of SiPMs considered still increases the number of scintillation events detected if compared with the 3 SiPMs PCB used for the positioning test (which has an identical circuit concept and was operated using same powering voltage and trigger on the output voltage variation). It is also important to note that the signal measured during the first acquisition campaign using muons as energetic particles (the one shown in figure 10) has an excellent signal-to-noise ratio even without being amplified by the CAEN N979.

In summary, the electronics is composed by $12 \times 13 = 156$ SiPMs, distributed on 13 identical PCBs, each one giving one or two independent outputs depending on the operation strategy, for a total of 13 or 26 signals. Since the selected fast amplifier provides 16 input channels, SARA will use one or two N979 modules, depending on the operating mode, and the required number of digitizers will be two or four. In both cases, a single CAEN DT5485PB power supply will be used thanks to the custom-made power switch.

3.6 Performance optimization

Regarding the performance of the scintillators, two goals were considered: to maximize the amount of light reaching the SiPMs and to prevent external light infiltrations. To this purpose, all six faces of the rectangular

2026 JINST 21 P01022

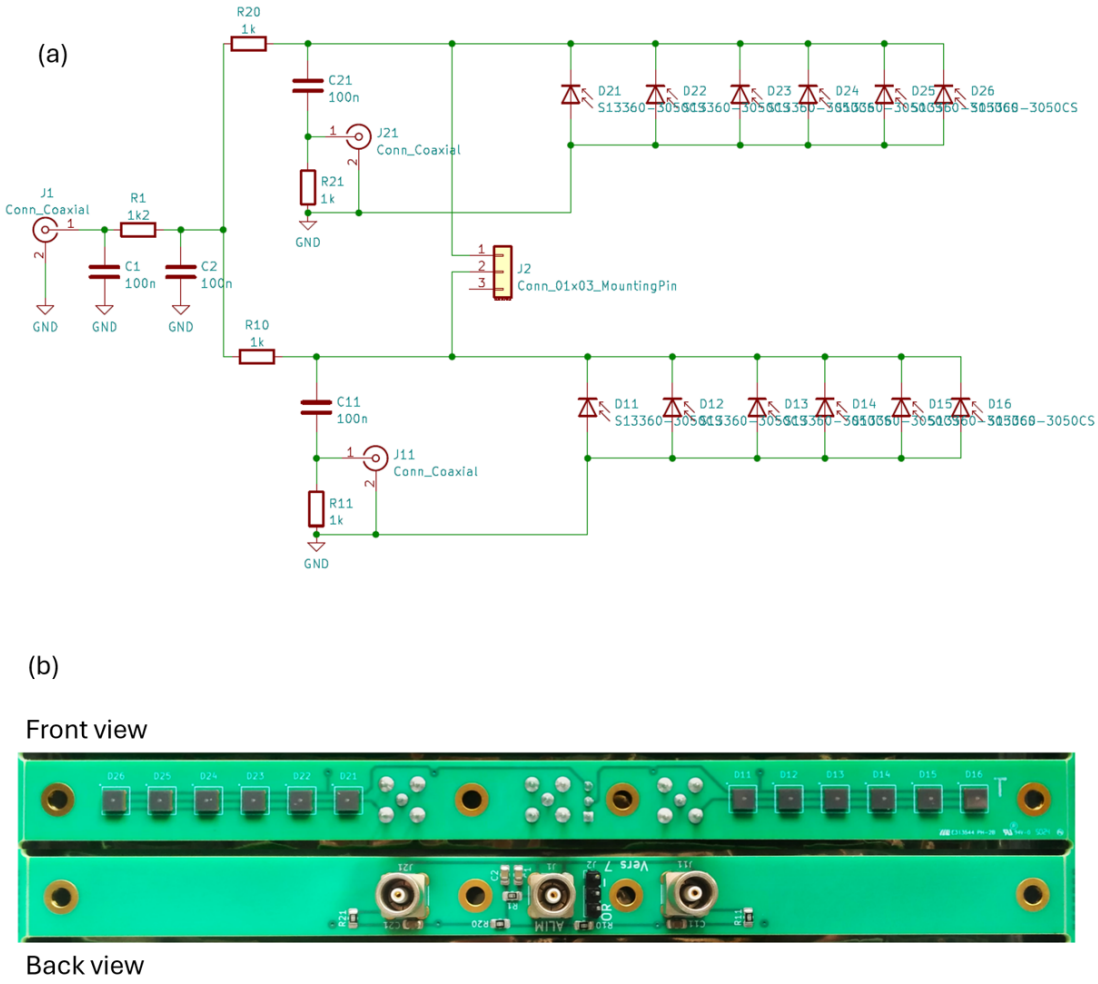

Figure 8. (a) PCB scheme. (b) Front and back views of a manufactured PCB.

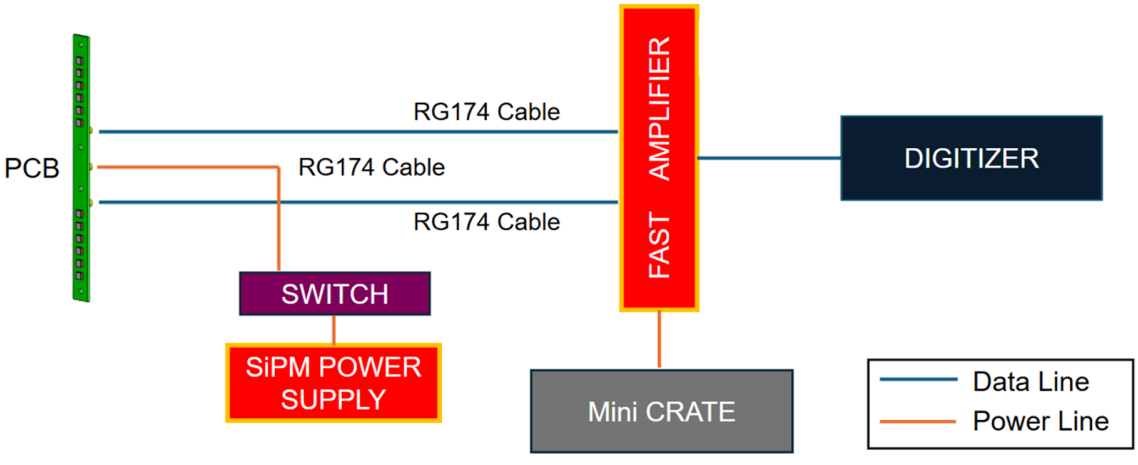

Figure 9. Scheme of the electronics architecture.

2026 JINST 21 P01022

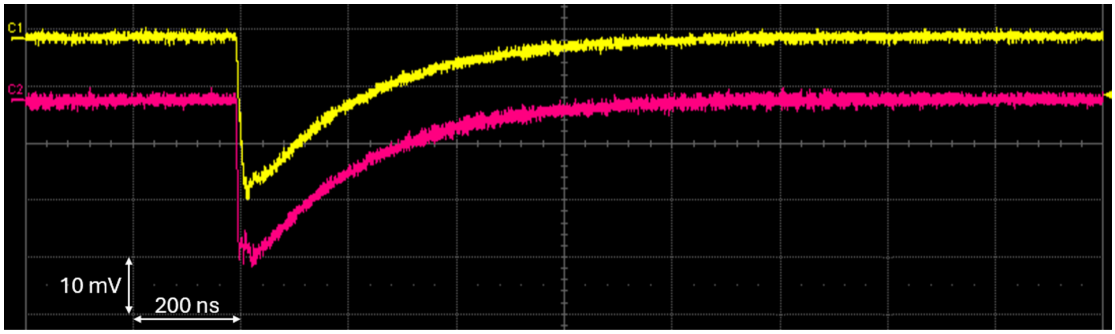

Figure 10. The average output obtained from the two channels of a scintillator when operated in parallel mode.

scintillator panels were polished and wrapped with aluminum foil with the reflective side facing inward; the aluminum reflective surface was cleaned and flattened before the application. Then, after the integration of aluminum foil and PCB, the scintillators were covered with an obscuring material, as commonly done for plastic scintillators. Specifically, the one selected was the OPAQ-1152i from Luminis Films, a black PVC foil designed to block visible light. Its selection was justified by the results of its absorbance characterization. The absorbance was measured by the spectrophotometer used — a PerkinElmer Lambda 650 — as:

$$A(f) = \log_{10} \frac{\Phi_R(f)}{\Phi_S(f)} \tag{3.1}$$

where $\Phi_R(f)$ is the intensity as function of the frequency of a reference light ray and $\Phi_S(f)$ is the intensity of an identical light ray after it pierced the tested material. The reference light was generated by the spectrophotometer combining a deuterium and a halogen lamps, whose resulting light was manipulated by a series of two monochromators to get the frequency dependence. In addition, two identical beams were obtained by the device exploiting an internal beam splitter. The results of the test (figure 11) show a rapid increment of the absorbance when moving toward lower wavelengths, before the instrument reaches saturation and starts to give unreliable values. According to the results, the chosen light protection material has an absorbance greater than 6 in the region of the visible spectrum, so it is tailored for its obscuration role.

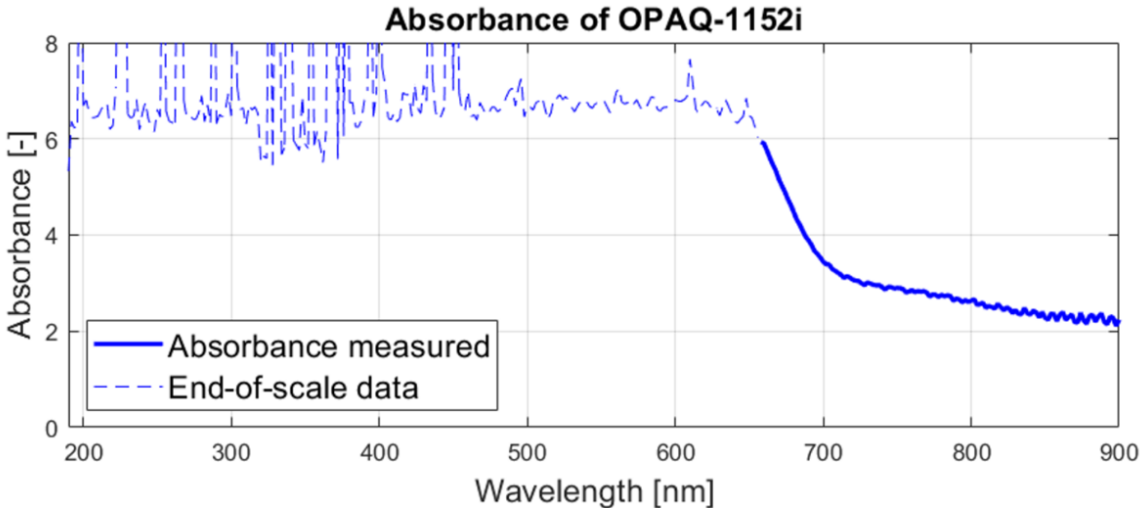

Figure 11. OPAQ-1152i absorbance measured with a PerkinElmer Lambda 650 spectrophotometer.

2026 JINST 21 P01022

4 Commissioning

After the conclusion of the design phase, the construction process started, yielding the results shown in the following figures. Figures 12-1 and 2 show some scintillators after the polishing process and some others wrapped in the aluminum foil; the rectangular holes allow the optical contact between SiPMs and scintillator. A scintillator with its detectors PCB secured with black adhesive tape and three completed scintillators are shown in figures 12-3 and 4. Figures 12-5 and 6 show some corner elements with ensats already hot-inserted and the first completed SARA box (the central one). Finally, figure 13 shows the whole instrument before the completion of the PCBs integration.

Figure 12. Construction process of the SARA scintillation detector. 1. Some of the polished scintillator panels. 2. Some scintillators wrapped in aluminum. 3. A PCB applied on a scintillator. 4. Three scintillators wrapped in OPAQ-1152i. 5. Some corner elements with ensats. 6. The first completed box.

2026 JINST 21 P01022

Figure 13. The instrument before the completion of the PCB integration.

Concerning the efficiency of the scintillators, the measurement procedure exploited the fact that the scintillators composing the boxes come in just two sizes, with eight elements in the first set (316 mm long panels) and four elements in the second (270 mm long panels). By stacking three scintillators from the same set and using the double coincidence between the top and bottom ones as proof that a muon crossed the whole stack, the efficiency of the middle panel can be evaluated as the ratio between the number of triple coincidences (all three scintillators triggered) and the one of double coincidences (only reference panels triggered). This procedure was performed testing each scintillator of the two sets and the efficiency of the final panel (that comes in a unique piece) was similarly measured by inserting it between two scintillators from the first set (316 mm). The coincidence counting has been achieved by assembling three identical readout channels, each one composed by a delay line amplifier (AMETEK® ORTEC® 460 [20]) and a single-channel discriminator (AMETEK® ORTEC® 551 [21]). The amplifier received the signals from a scintillator and its unipolar output was sent to the discriminator, whose lower threshold was tuned to accept only the events with highest energies in order to cut most of the noise. The two identical outputs of each discriminator were then sent to two AMETEK® ORTEC® 414A Fast Coincidence [22] units, one receiving input from all three scintillators and the other one from the two reference panels only; in this way, the two counts were referred to the same events. Finally, two dual counter-timer (AMETEK® ORTEC® 994 [23]) received the signals from each coincidence unit for the counting. The efficiency measurement setup is represented in figure 14 and the results of the analysis are collected in table 5. These values, together with those shown in table 2 from section 3.2, were used to compute the overall efficiencies of the system modules. In particular, the latter were obtained by multiplying the average efficiency value of the scintillators of a module with the corresponding percentage of solid angle covered, obtaining the percentage of revealed annihilation products. The results are collected in table 6. According to them,

2026 JINST 21 P01022

it is possible to conclude that the system satisfies the second requirement and shows good overall efficiency for measuring coincidences, e.g., those due to the two antiparallel photons emitted during the annihilation between the $\bar{H}$ positron and one of the grating electrons.

The dark current was measured for one of the PCBs, connected to the same power supply of the others, but not applied to any scintillator. The PCB was placed into a small box wrapped in multiple layers of obscuring material to prevent any possible influence of stray light. The result of the measurement, equal to 1.15 µA, is in agreement with the datasheet supplied by Hamamatsu.

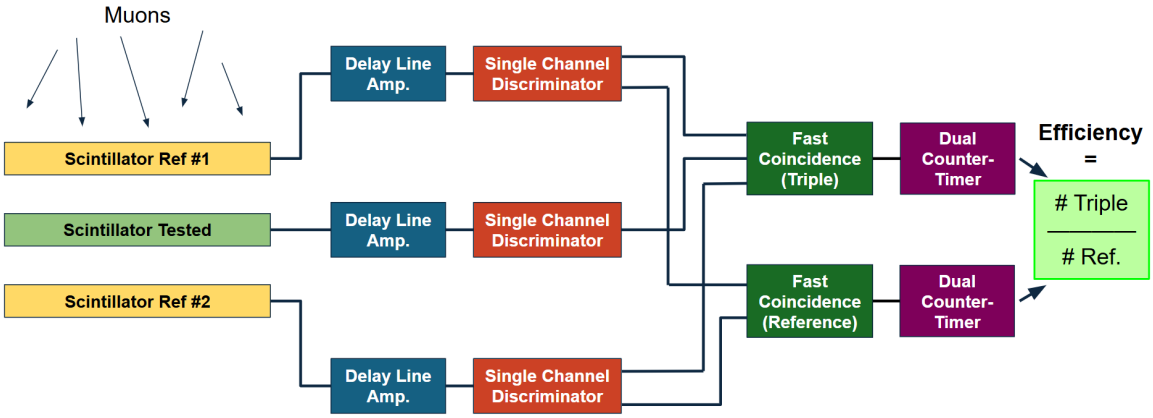

Figure 14. Scintillator efficiencies measurement setup.

Table 5. The scintillators efficiency. In the brackets is specified the position of the scintillator: two digits for the box and the acronyms Lat., Low., Upp. and Last for the position inside the module (Lateral, Lower, Upper, Last panel).

Scintillator	Efficiency measured	:	Scintillator	Efficiency measured
1 (01_Upp)	0.84 ± 0.04	:	8 (02_Low)	0.76 ± 0.04
2 (02_Lat)	0.87 ± 0.04	:	9 (03_Upp)	0.77 ± 0.04
3 (02_Lat)	0.79 ± 0.04	:	10 (03_Lat)	0.84 ± 0.04
4 (01_Low)	0.86 ± 0.04	:	11 (03_Lat)	0.79 ± 0.04
5 (02_Upp)	0.82 ± 0.04	:	12 (03_Low)	0.81 ± 0.04
6 (01_Lat)	0.89 ± 0.04	:	13 (Last)	0.80 ± 0.04
7 (01_Lat)	0.84 ± 0.04	:		

Table 6. The overall system detection capabilities. The % of Solid Angles come from table 2 and the averaged measured efficiencies of the modules were evaluated exploiting the values contained in table 5.

Module	% of Solid Angle	Avg. measured Efficiency	% of Detected Particles
First Box	66.2	0.86	56.9
Second Box	64.1	0.81	51.9
Third box plus Final Panel	71.1	0.80	56.9

2026 JINST 21 P01022

5 Conclusions

This article describes the design, development and commissioning of SARA (Scintillator Assemblies to Reveal Annihilations), the scintillation detector array created for the time-of-flight measurement of antihydrogen atoms within the moiré deflectometer gravity detector of the AEgIS experiment. The process aimed at realizing a simple yet effective instrument, complementary to the state-of-the-art OPHANIM detector in measuring the gravity acceleration acting on antimatter. In more detail, the detector is composed of three independent modules, and the arrangement of the scintillators in boxes makes it possible to form coincidences between them, allowing both the detection of annihilation signals and the simultaneous minimization of noise, mainly due to cosmic muons. The two-part box architecture effectively allows for assembly and disassembly of the boxes. Furthermore, the alignment between the various corner elements at the two parts conjunctions is satisfactory, since it guarantees the insertion of the fastening screws for all the three boxes. The choice to standardize the corner elements allows the box components to be symmetric, giving the possibility to rotate by 180° both the upper and lower parts with respect to the vertical axis, choosing in which direction the PCB output ports are oriented (along the deflectometer axis). This feature allows minimization of the lengths of the cables from the power supply and to the fast amplifiers. From a structural perspective, it has been demonstrated, first with the finite element simulations performed to validate the design (described in section 3.4) and later with the inspection of the final product, that SARA is structurally stiff and able to stand all the loads it will encounter during its operational life. Concerning the detector performance, the signal collected during the first acquisition of muons (the one shown in figure 10), indicates that the SiPMs coupled to the scintillators have an excellent signal-to-noise ratio, even before amplification by the fast amplifiers, and a rise time below 10 ns. Moving to the overall detector efficiency, its characterization showed satisfactory results. Indeed, all the three modules guarantee a percentage of detected annihilation products higher than 50%, and the cross detection among the three modules is negligible, as can be deduced from table 2. Taking stock of everything that has been presented, it can be concluded that SARA will be able to accomplish its objective, enabling the time-of-flight measurement of the antihydrogen beam, a crucial step towards the first in-beam measurement of antimatter gravitational free fall.

Acknowledgments

The donation of plastic scintillators from the concluded ATRAP collaboration is gratefully acknowledged. Professor Alberto Rotondi is here gratefully acknowledged for all his enlightening suggestions. Special thanks are extended to Veronica Marzo for her contribution to the efficiency measurement. The project was funded by Politecnico di Milano.

References

[1] AEgIS collaboration, *Proposed antimatter gravity measurement with an antihydrogen beam*, *Nucl. Instrum. Meth. B* **266** (2008) 351 [arXiv:2306.04594].

[2] M. Charlton, S. Eriksson and G.M. Shore, *Antihydrogen and Fundamental Physics*, Springer (2020) [DOI:10.1007/978-3-030-51713-7].

[3] L. Zehnder, *Ein neuer Interferenzrefraktor*, *Z. Instrument.* **11** (1891) 275.

2026 JINST 21 P01022

[4] L. Mach, *Ueber einen Interferenzrefraktor*, *Z. Instrument.* **12** (1892) 89.

[5] AEgIS collaboration, *A moiré deflectometer for antimatter*, *Nature Commun.* **5** (2014) 4538.

[6] M.K. Oberthaler et al., *Inertial sensing with classical atomic beams*, *Phys. Rev. A* **54** (1996) 3165.

[7] AEgIS collaboration, *Real-time antiproton annihilation vertexing with submicrometer resolution*, *Sci. Adv.* **11** (2025) ads1176 [arXiv:2406.16044].

[8] C. Amsler et al., *Pulsed production of antihydrogen*, *Commun. Phys.* **4** (2021) 19.

[9] AEgIS collaboration, *High-yield thermalized positronium at room temperature emitted by morphologically tuned nanochanneled silicon targets*, *J. Phys. B* **54** (2021) 085004.

[10] M. Charlton, *Antihydrogen production in collisions of antiprotons with excited states of positronium*, *Phys. Lett. A* **143** (1990) 143.

[11] P. Moskal et al., *Positronium image of the human brain in vivo*, *Sci. Adv.* **10** (2024) eadp2840.

[12] Z. Zhang, *The Detection of Cold Antihydrogen Atoms*, Ph.D. thesis, Ruhr University, Bochum, Bochum, Germany (2007).

[13] S. España et al., *Performance evaluation of SiPM photodetectors for PET imaging in the presence of magnetic fields*, *Nucl. Instrum. Meth. A* **613** (2010) 308.

[14] https://luxiumsolutions.com/radiation-detection-scintillators/plastic-scintillators/bc400-bc404-bc408-bc412-bc416.

[15] E.M. Quintos, C.H. Zepeda Fernández, L.F.R. Herrera and E.M. Barbosa, *Intrinsic time resolution and efficiency study for simulated scintillators plastics with Geant4*, *Rev. Mex. Fis.* **69** (2023) 040901.

[16] Material data sourced from Weerg, https://www.weerg.com/3d-printing-materials/nylon/pa-12-classic.

[17] https://www.caen.it/products/dt5485p/.

[18] https://www.caen.it/products/n979/.

[19] https://www.caen.it/products/dt5725/.

[20] https://www.ortec-online.com/products/electronic-instruments/amplifiers/460.

[21] https://www.ortec-online.com/products/electronic-instruments/single-channel-analyzers/551.

[22] https://www.ortec-online.com/products/electronic-instruments/delays-and-gates/414a.

[23] https://www.ortec-online.com/products/electronic-instruments/counters-timers-and-ratemeters/994.

2026 JINST 21 P01022